RESEARCH ARTICLE

Environmental Remediation

Energy & Environmental Materials WILEY

Self-Floating Efficient Solar Steam Generators Constructed Using Super-Hydrophilic N,O Dual-Doped Carbon Foams from Waste Polyester

Huiying Bai, Ning Liu, Liang Hao, Panpan He, Changde Ma, Ran Niu, Jiang Gong, and Tao Tang**

Solar evaporation is recognized as a prospective technique to produce freshwater from non-drinkable water using inexhaustible solar energy. However, it remains a challenge to fabricate low-cost solar evaporators with obviously reduced water evaporation enthalpy to achieve high evaporation rates. Herein, N,O dual-doped carbon foam (NCF) is fabricated from the low-temperature carbonization of poly(ethylene terephthalate) (PET) waste by melamine/molten salts at 340 °C. During carbonization, melamine reacts with carboxylic acids of PET degradation products to yield a crosslinking network, and then molten salts catalyze the decarboxylation and dehydration to construct a stable framework. Owing to rich N,O-containing groups, 3D interconnected pores, super-hydrophilicity, and ultra-low thermal conductivity (0.0599 W m^{-1} K^{-1}), NCF not only achieves high light absorbance (ca. 99%) and solar-to-thermal conversion, but also promotes the formation of water cluster to reduce water evaporation enthalpy by ca. 37%. Consequently, NCF exhibits a high evaporation rate (2.4 kg m^{-2} h^{-1}), surpassing the-state-of-the-art solar evaporators, and presents good anti-acid/basic abilities, long-term salt-resistance, and self-cleaning ability. Importantly, a large-scale NCF-based outdoor solar desalination device is developed to produce freshwater. The daily freshwater production amount per unit area (6.3 kg) meets the two adults' daily water consumption. The trash-to-treasure strategy will give impetus to the development of low-cost, advanced solar evaporators from waste plastics for addressing the global freshwater shortage.

1. Introduction

Energy crisis and freshwater shortage have become two of most serious issues in our modern society. As 97% of water resources on the Earth belong to seawater, the desalination of seawater to obtain freshwater is actively pursued to tackle with the global water shortage, particularly in the water-stress and remote regions.[1] Traditional methods such as reverse osmosis feature high capacity for water production but are energy intensive. In recent decades, the development and utilization of inexhaustible, green solar energy have attracted extensive attention for diverse applications.[2–5] Solar evaporation has been recognized as one of most promising techniques to produce freshwater from seawater. However, conventional approaches for solar evaporation directly heat bulk water, inevitably leading to the obvious heat loss. By contrast, an interfacial solar-driven steam generation device with a floating structure, which conducts thermal localization at the gas-liquid interface, can avoid the obvious heat loss and realize high conversion efficiency.[6–14] As the key component of such system, a solar absorber should possess several characteristics, e.g., high and broadband light absorption, super-hydrophilicity, ultra-low thermal conductivity, porous channels for water transfer, and good photothermal conversion. Typical photothermal materials include polymer,[15–18] plasma material,[19–21] semiconductor,[22] and carbon material.[23–25]

Carbon foam, which combines the intrinsic advantages of tailored porous structures and carbon materials, has attracted ever-increasing interest as an advanced photothermal material.[26] Firstly, the porous structure with rough morphology reduces light reflection and enhances light scattering inside pores to improve solar energy utilization.[27] Secondly, porous characteristics induce a low thermal conductivity, which effectively reduce heat loss by localizing the produced heat in the interfacial region of water and air.[28] Thirdly, interconnected porous architecture offers many channels for realizing efficient vapor escaping and water transport. Lastly, owing to light-weight property, carbon foam can float on the surface of water without any supports. So far, great progress has been achieved to

H. Bai, N. Liu, L. Hao, P. He, Prof. R. Niu, Prof. J. Gong
Key Laboratory of Material Chemistry for Energy Conversion and Storage, Ministry of Education, Hubei Key Laboratory of Material Chemistry and Service Failure, Hubei Engineering Research Center for Biomaterials and Medical Protective Materials, School of Chemistry and Chemical Engineering, Huazhong University of Science and Technology, Wuhan 430074, China
Dr. C. Ma, Prof. T. Tang, Prof. J. Gong
State Key Laboratory of Polymer Physics and Chemistry, Changchun Institute of Applied Chemistry, Chinese Academy of Sciences, Changchun 130022, China
E-mail: ttang@ciac.ac.cn
E-mail: gongjiang@hust.edu.cn
The ORCID identification number(s) for the author(s) of this article can be found under https://doi.org/10.1002/eem2.12235.

DOI: 10.1002/eem2.12235

synthesize carbon foams for interfacial solar-driven steam generation by using freeze-drying/carbonization,[29,30] acid-catalyzed carbonization,[31] surface coating,[32] pyrolysis,[33] etc. Nevertheless, most of carbon foams suffer from unsatisfactory evaporation rates (e.g., <1.6 kg m^{-2} h^{-1} under 1 kW m^{-2} irradiation), complex fabrication procedures, and high cost. Recently, a new strategy of reducing water evaporation enthalpy has been reported to improve the evaporation rate of polymer gels.[34–36] This is because the hydrophilic groups of polymer form numerous hydrogen bonds with water molecules to favor for the formation of water cluster, which needs less energy for liquid-to-vapor water process than bulk water. In this context, reducing water evaporation enthalpy of carbon foam by introducing abundant hydrophilic functional groups seems a promising way to significantly enhance the evaporation rate, which however has not been touched yet.

On the other hand, millions of tons of urban and industrial plastics are discarded annually, which bring about serious environmental problems (e.g., "white pollution") and significant waste of resources. Converting waste plastics into high value-added products has aroused wide attention.[37–39] Since plastics usually possess a high content of carbon element, upcycling plastic wastes into functional carbon materials is regarded as one of most hopeful approaches to deal with waste plastics. Typically, Jie et al. reported the microwave catalytic deconstruction of various plastic feedstocks into carbon nanotube.[40] Luong et al. utilized the flash Joule heating of plastic waste at 3000 K to prepare graphene.[41] During the last two decades, we have proposed three strategies (i.e., combined catalysis, active template, and fast carbonization) to convert waste plastics into carbon nanomaterials (e.g., carbon nanotube and graphene) for photocatalysis, supercapacitors, etc.[42–46] However, all of these previous methods suffer from high carbonization temperature (e.g., >700 °C) and high energy-consumption. From the perspectives of sustainable development and solar energy exploitation, synthesizing low-cost carbon-based solar evaporators from waste plastics can kill two birds with one stone. Recently, we reported the carbonization of waste plastics at 550 °C into porous carbon powder for solar evaporation.[47–49] Unfortunately, previous solar evaporators showed low evaporation rates (e.g., <1.7 kg m^{-2} h^{-1} under 1 kW m^{-2} irradiation) and required tedious procedures (e.g., vacuum filtration and dip coating) for further processing and molding of carbon powder. Additionally, as far as we know, there have been no studies on the synthesis of carbon foams from waste plastics. Thereby, directly transforming waste plastics into self-floating, low-cost carbon foams as solar evaporators that show low water evaporation enthalpy and high evaporation rates is particularly attractive to simultaneously address global freshwater shortage and eliminate waste plastics.

In this work, N,O dual-doped carbon foam (NCF) is facilely synthesized from the low-temperature carbonization of waste PET by utilizing melamine/eutectic salts at 340 °C. Melamine and eutectic salts show a synergetic effect on the growth of NCF, in which the in-situ formed low molecule compounds (e.g., CO_2 and H_2O) act as foaming agents to construct 3D interconnected pores. With the combined merits of self-floating, lightweight, interconnected porous structure, ultra-low thermal conductivity, super-wetting, and super-hydrophilicity, NCF displays high light absorption, good solar-to-heat conversion, and low water evaporation enthalpy. Accordingly, NCF exhibits a notably high evaporation rate (2.4 kg m^{-2} h^{-1}) under 1 kW m^{-2} irradiation.

2. Results and Discussion

2.1. Morphology, Microstructure, and Phase Structure of NCF

N,O dual-doped carbon foam was prepared through the low-temperature carbonization of PET by utilizing melamine and molten salts ($ZnCl_2$/NaCl) at 340 °C (**Figure 1**). Melamine reacts with carboxylic acids of PET degradation products to yield a crosslinking network, then molten salts catalyze the decarboxylation and dehydration for constructing a more stable framework, owing to the Lewis acidity of $ZnCl_2$.[50] NCF is ultra-lightweight and displays a low apparent density of ca. 8.6 mg cm^{-3}, as proved by one piece of NCF with a size of ca. 7.9 × 7.8 × 3.3 cm^3 standing on a twig, without bending the twig (**Figures 2**a and Figure S1). SEM images of NCF display an open-cell,

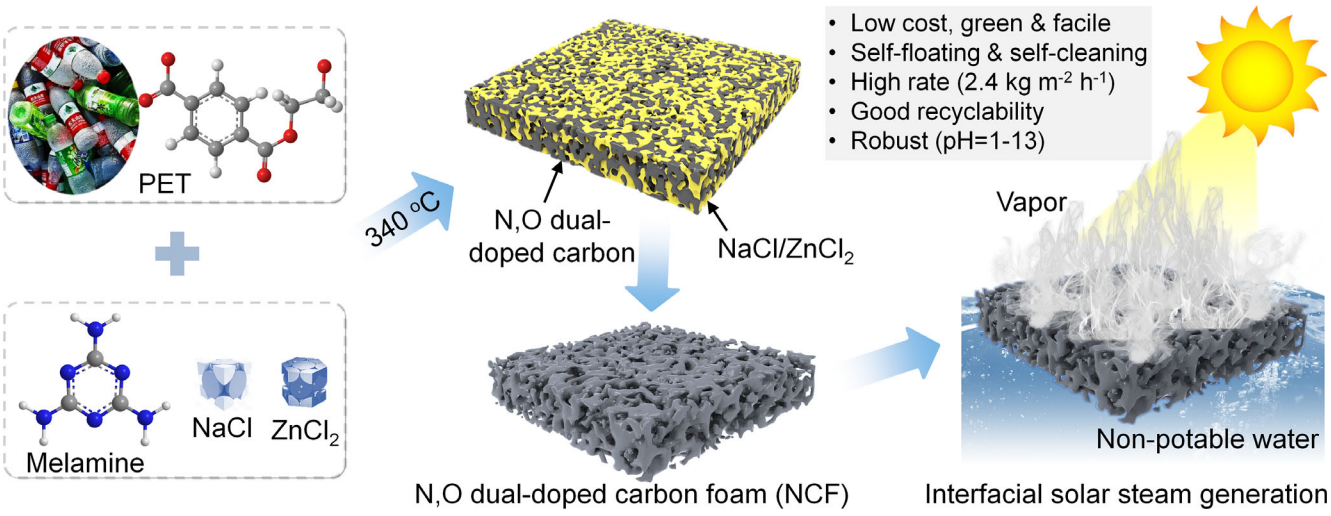

Figure 1. Scheme of the low-temperature carbonization of PET to prepare NCF for interfacial solar evaporation.

interconnected porous structure, and pores in a size ranging from tens of microns to hundreds of microns are clearly observed (Figure 2b). The walls of pores are overall tens of microns in thickness and possess many micron pores (Figure 2c). The porous structure of NCF was further analysed by N_2 physisorption at 77 K and mercury intrusion measurements (Figures S2 and S3). NCF displays a low specific surface area of ca. 36 m^2 g^{-1} and possesses some micropores/ mesopores/macropores as well as many micron-sized pores with a size of 30–160 μm.

In comparison with that of the dense products from PET carbonization by utilizing merely melamine or molten salts (Figure S4), it can be concluded that these 3D interconnected pores are related to the physical template effect of molten salts and foaming effect of in situ–formed small molecular compounds (e.g., H_2O and CO_2) in the degradation and crosslinking processes. Besides, the carbonization temperature and mass ratio of melamine/PET are pivotal for the growth of NCF (Table S1). For example, if the carbonization temperature is below 340 °C or the melamine/PET mass ratio is below 0.5, PET still remains in the carbon products, meaning the incomplete carbonization of PET (Figures S5 and S6). After increasing the carbonization temperature above 400 °C, N,O dual-doped carbon powder instead of NCF is obtained (Figure S7),[50] indicating that lower carbonization temperature is advantageous for the foaming process. To further clarify the PET carbonization mechanism using melamine and $ZnCl_2$/NaCl, model experiments were conducted, in which PET, PET-melamine mixture, PET-melamine-NaCl mixture, and PET-melamine-$ZnCl_2$/NaCl mixture were heated at 280 °C for 10 min in the crucible and then characterized by FT-IR (Figures S8 and S9). The results confirm the amide reaction between the amino group of melamine and the carboxyl group of carboxyl-terminated PET degradation products. Besides, $ZnCl_2$ not only promotes the decarboxylation or decarbonylation of amide, ester, and carboxyl in the melamine-crosslinked PET degradation intermediates, but also accelerates the dehydration to form double bond.

The elemental mapping based on energy-dispersive X-ray (EDX) spectroscopy of NCF depicts uniform element distribution of carbon, nitrogen, and oxygen (Figure 2d–f). The HRTEM image displays many discontinuous graphitic sheets with a low degree of ordering (Figure 2g), which reveals the low graphitization degree of NCF. The interplanar spacing of ca. 0.36 nm is larger than that of graphite

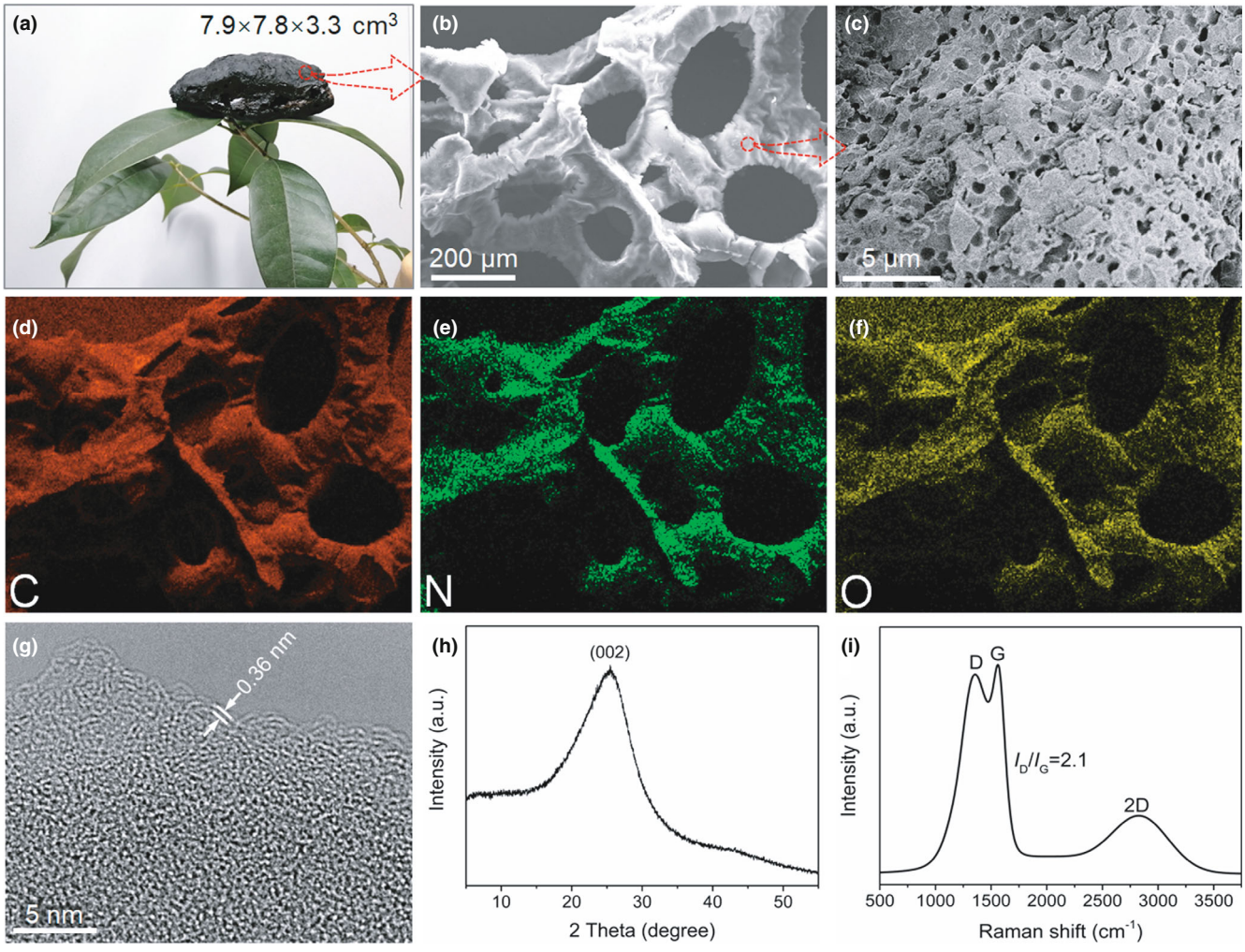

Figure 2. a) Photograph of one piece of NCF standing on a twig, proving lightweight performance. b, c) SEM images of NCF. EDX maps of NCF for d) carbon, e) nitrogen and f) oxygen elements according to the b) SEM image. Note: NCF was stuck on the surface of carbon-based conductive adhesive tape during testing. g) HRTEM image, h) XRD pattern and i) Raman spectrum of NCF.

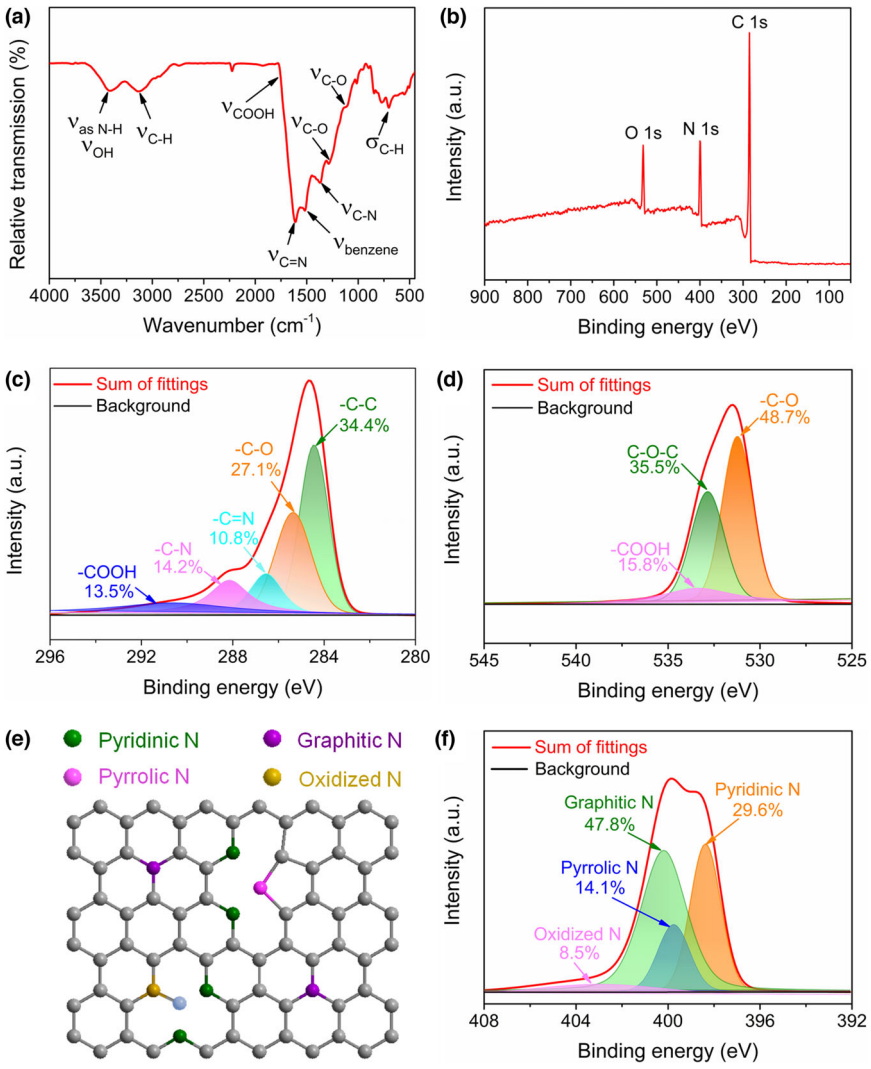

Figure 3. a) FT-IR curve and b) XPS spectrum of NCF. High-resolution c) C 1s and d) O 1s XPS spectra of NCF. e) Scheme of different N species in NCF. f) High-resolution N 1s XPS spectrum of NCF.

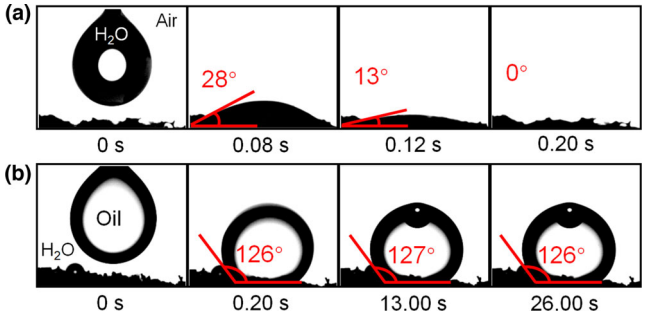

Figure 4. Time evolution of a) water or b) oil contact angles of NCF.

(0.34 nm), likely due to the introduction of nitrogen and oxygen atoms in the graphitic framework. XRD and Raman were applied for characterizing the crystalline structure of NCF. The broad peak at $2\theta = 18°–32°$ is attributed to the graphitic (002) plane (Figure 2h), confirming the low graphitization degree. The Raman spectrum of NCF displays three characteristic peaks (Figure 2i), including D peak at 1358 cm^{-1}, G peak at 1561 cm^{-1}, and 2D peak at 2760 cm^{-1}, which are assigned to defect carbon, sp^2-hybridized graphitic carbon, and two phonons with opposite momentum in the highest optical branch, respectively.[51,52] The ratio of G to D (I_D/I_G) provides an effective index to compare lattice defects and graphitization degree. The high I_D/I_G value of NCF (2.1, Figure S10) indicates the existence of many randomly arranged graphitic sheets, in accordance with the results of HRTEM and XRD (Figure 2g,h).

2.2. Functional Groups, Elemental Composition, and Hydrophilicity of NCF

Fourier-transform infrared was employed to characterize the functional groups of NCF (**Figure 3**a). The peak at 3416 cm^{-1} is owing to the OH stretching vibration and NH asymmetric stretching vibration. The peaks at 3119 and 1740 cm^{-1} are due to the stretching vibration of C–H and COOH, respectively. The peaks at 1609 and 1366 cm^{-1} are attributed to the C=N stretching vibration and benzene stretching vibration, respectively. The peaks at 1280 and 1114 cm^{-1} correspond to the C–O stretching vibration. XPS spectrum (Figure 3b) indicates that the surface of NCF contains carbon (72.8%), nitrogen (18.0%), and oxygen (9.2%) elements, which are close to the result of elemental analysis (C: 69.8%, N: 17.2%, O: 9.0%, H: 4.0%). The high-resolution C 1s XPS spectrum is deconvolved into five single peaks (Figure 3c): COOH (290.8 eV, 13.5%), C–N (288.1 eV, 14.2%), C=N (286.5 eV, 10.8%), C–O (285.3 eV, 27.1%), and graphitic carbon (284.4 eV, 34.4%).[53] The high-resolution O 1s XPS spectrum is curve-fitted into three peaks (Figure 3d): COOH (533.3 eV, 15.8%), C–O–C (532.8 eV, 35.5%), and C–O (531.3 eV, 48.7%). The high-resolution N 1s XPS spectrum is deconvolved four peaks (Figure 3e,f): oxidized N (403.3 eV, 8.5%), graphitic N (400.2 eV, 14.1%), pyrrolic N (399.6 eV, 47.8%), and pyridinic N (398.3 eV, 29.6%).[54] Hence, NCF possesses rich N- or O-containing functional groups.

The hydrophilicity and lipophobicity of NCF were analyzed by water and oil (i.e., dichloromethane) contact angles, respectively. The initial water contact angle is ca. 28° at 0.08 s and quickly falls down to 0° within 0.2 s (**Figure 4**a, Video S1). In comparison, the contact angle of an oil drop on the surface of water-immersed NCF remains as high as ca. 126° for at least 26 s (Figure 4b, Video S2). Addtionally, the water uptake rate of NCF is ca. 50%, which is evidently higher than that of NC@PVDF (ca. 13%). The results above prove the superhydrophilicity, good wettability, super-lipophobicity, and high water uptake rate of NCF, which are likely thanks to the combination of rich N,O-containing functional groups and 3D interconnected pores.

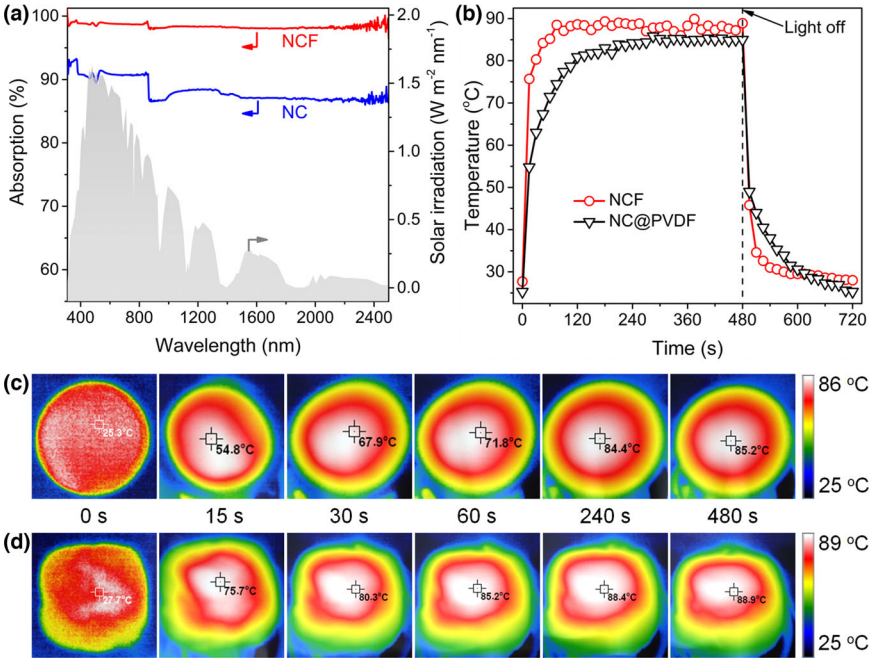

Figure 5. a) UV-Vis-NIR absorption spectra of NCF and NC. b) Surface temperature and c) infrared images of NCF and NC@PVDF under 1 kW m^{-2} irradiation.

Undoubtedly, the super-hydrophilicity of NCF favors for rapid water transport and vapor escaping, meanwhile the lipophobicity enhances the anti-fouling and self-cleaning abilities of NCF for solar steaming oil/water mixture.

2.3. Interfacial solar-driven steam generation

It is widely accepted that ideal photothermal materials should own characteristics of broadband and high light absorption, high porosity for water transport and vapor escaping, ultra-low thermal conductivity, and good solar-to-heat conversion ability. Consequently, the UV-Vis-NIR spectrometer was firstly employed to characterize the light absorption of NCF. Remarkably, NCF exhibits a broadband and high light absorption of 98%–99% (**Figure 5**a), obviously higher than that of N, O dual-doped carbon foam (NC) powder (87%–88%), which was obtained by grinding NCF. Since the chemical components of NCF and NC are same, the higher light absorption of NCF than NC is likely ascribed to the 3D porous structure of NCF, which favors for light multiple scattering. Meanwhile, the ultra-low thermal conductivity of NCF (0.0599 W m^{-1} K^{-1}) can reduce heat loss (Note S1). The alliance of high light absorption and low thermal conductivity is beneficial for photothermal conversion. To certify such deduction, the surface temperature of NCF was recorded (Figure 5b–d). Under 1 kW m^{-2} irradiation, the surface temperature of NCF rises rapidly from 27.7 to 88.4 °C within 4 min and subsequently remains the stable temperature of ca. 88.9 °C. By contrast, the hydrophilic poly(vinylidene fluoride) (PVDF) filtrate membrane supported NC powder (noted as NC@PVDF) shows relatively lower surface temperature of ca. 85.2 °C with a slower heating rate. The comparison result demonstrates the good solar-to-thermal conversion ability of NCF.

The evaporation performance of NCF was studied by employing a lab-made measurement system (Figure S11). The water mass reduction under 1 kW m^{-2} irradiation is approximately linear with irradiation time (**Figure 6**a). Upon 60 min irradiation, the water evaporation rate of NCF is measured to be 2.4 kg m^{-2} h^{-1} (Figure 6b, Video S3), which is apparently higher than that of water in darkness (0.4 kg m^{-2} h^{-1}) or under 1 kW m^{-2} (0.86 kg m^{-2} h^{-1}), or water using NC@PVDF (1.27 kg m^{-2} h^{-1}) under 1 kW m^{-2} irradiation. Therefore, NCF shows superb performance in interfacial solar evaporation. Moreover, the irradiation intensity (0.5–3 Sun) markedly influences the water evaporation performance of NCF (Figure 6c,d). For instance, the evaporation rate of NCF increases dramatically from 1.32 kg m^{-2} h^{-1} (0.5 Sun) to 4.26 kg m^{-2} h^{-1} (3 Sun), which are higher than those of NC@PVDF, e.g., 0.86 kg m^{-2} h^{-1} (0.5 Sun) and 3.43 kg m^{-2} h^{-1} (3 Sun), as shown in Figure S12. Meanwhile, the steady surface temperature of NCF goes up from 50.6 °C (0.5 Sun) to 70.8 °C (3 Sun), as displayed in Figure S13. It is worthy of note that the water evaporation rate of N,O dual-doped carbon foam obtained from the cabronization of waste PET by melamine/molten salts at 340 °C (marked as W-NCF) is measured as 2.37 kg m^{-2} h^{-1} under 1 kW m^{-2} irradiation, indicating that W-NCF also works very well in solar steaming.

To measure the water evaporation enthalpy, the water loss in the dark within 1 h was recorded, in which the evaporators receive the same energy from the environment to convert liquid water to vapor.[34,55,56] As shown Figure 6e, the water mass change using NCF is 669 mg, which is higher than that of water without NCF (419 mg). Considering the known theoretical evaporation enthalpy of liquid water (ca. 2.434 kJ g^{-1}), the enthalpy of NCF is calculated by the formula:

$$U_{in} = E_{equ} m_g = E_0 m_0 \quad (1)$$

where U_{in} is the total energy absorbed from the environment per hour; E_0 and m_0 refer to the water evaporation enthalpy (kJ g^{-1}) and the mass loss (g) of water in 1 h without NCF in the dark, respectively; m_g means the water loss (g) of NCF while E_{equ} is the equivalent evaporation enthalpy (kJ g^{-1}). The water evaporation enthalpy of NCF is calculated as 1.524 kJ g^{-1}, which is reduced by 37% compared to that of bulk water without NCF. Thereby, NCF can effectively reduce the water evaporation enthalpy, which is likely owing to the marriage of rich hydrophilic N,O-containing functional groups and 3D interconnected pores. Further discussion on the mechanism will be provided in the following section. Accordingly, the conversion efficiency of NCF is calculated to be 77.9% (0.5 Sun), 83.8% (1 Sun), 74.5% (1.5 Sun), 64.1% (2 Sun), 56.9% (2.5 Sun), and 54.5% (3 Sun), respectively (Figure S14), which are higher those of NC@PVDF, e.g., 55.5% (0.5 Sun) and 53.3% (3 Sun), as shown in Figure S12. More importantly, the evaporation rate of NCF surpasses many advanced solar evaporators

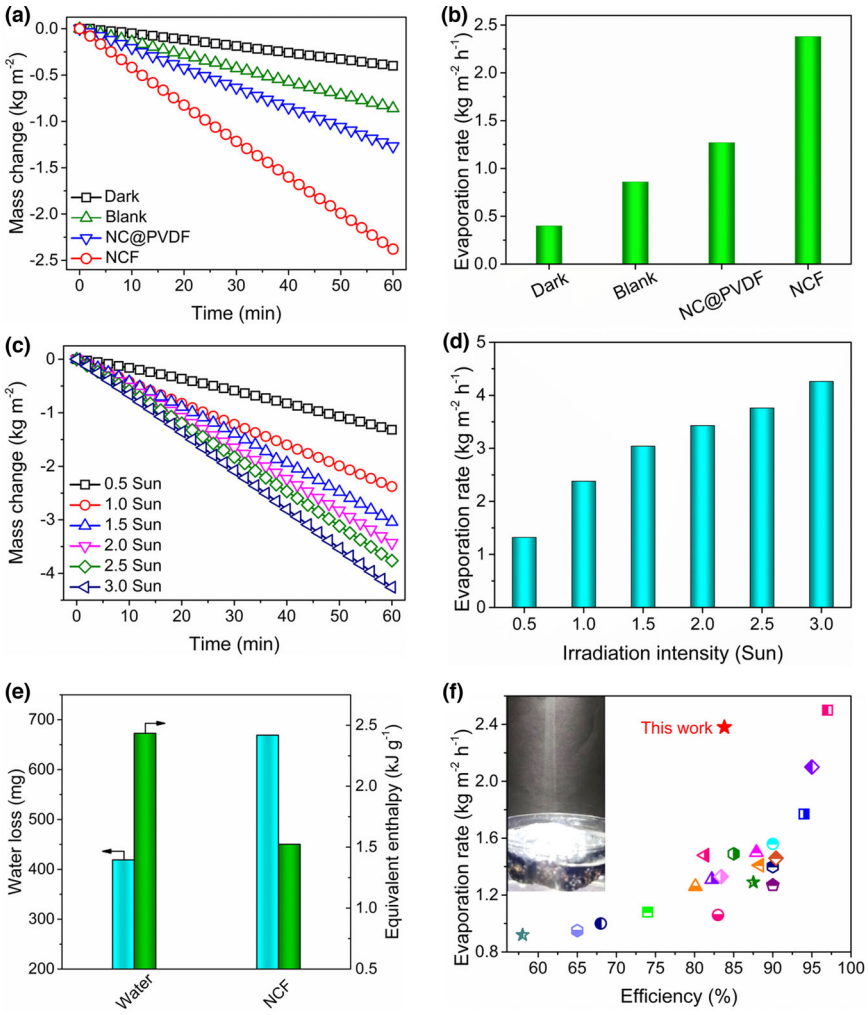

Figure 6. a) Cumulative water mass changes and b) evaporation rates under different conditions: in the dark (Dark), under 1 kW m^{-2} (Blank), with NC@PVDF under 1 kW m^{-2} (NC@PVDF), and with NCF under 1 kW m^{-2} (NCF). c) Cumulative water mass changes and d) evaporation rates of NCF under 0.5–3 Sun irradiation. e) Water mass changes and equivalent enthalpies of water and NCF. f) Comparison of the interfacial solar evaporation performance of NCF with some reported solar evaporators (Table S2). Note: the inset displays the photograph of NCF during solar evaporation.

(Figure 6f and Table S2), e.g., wood-based carbon foam (1.26 kg m^{-2} h^{-1}),[33] MXene hybrid (1.33 kg m^{-2} h^{-1}),[22] graphene foam (1.4 kg m^{-2} h^{-1}),[27] graphene oxide aerogel (1.62 kg m^{-2} h^{-1}),[28] porous carbon (1.68 kg m^{-2} h^{-1}),[47] and bilayer polyacrylamide aerogel (2.0 kg m^{-2} h^{-1}).[15]

Based on the results and discussion above, we put forwards the possible mechanism on the solar steam generation of NCF (**Figure 7**). Firstly, NCF owns the interconnected porous structures and thus can effectivley transport water from bulk water to the surface carbon layer via capillary force, which guarantees sufficient water supply for the evaporation. Secondly, the ultra-low thermal conductivity of NCF reduces the heat loss from the surface hot zone to the bottom water, which improves heat localization. Thirdly, the 3D interconnected pores endow NCF with a high light absorbance, which enhances the solar-to-thermal conversion. Fourthly, NCF possesses rich hydrophilic N,O-containing functional groups, which form hydrogen bonds with water molecules to yield the bonded water. Therefore, there are three types of water molecules in the NCF-based solar evaporation system, including free water, intermediate water, and the bonded water with NCF. The intermediate water forms hydrogen bonds with the bonded water, which weakens the hydrogen bonds among intermediate water molecules and is ultimately conducive to lower down the energy demand for the liquid-to-vapor water process. In this scenario, we suppose that part of water molecules in NCF evaporate in the form of water cluster.[55,57,58] To test such hypothesis, a model solar evaporation experiment was conducted using LiCl solution as Li^+ is easily loaded by water cluster. The Li^+ concentration in the condensed water using NCF is ca. 29 times higher than that of water without evaporators (Figure S15), confirming that the water steam escaping from NCF is in the form of water cluster. Similar phenomena are reported in previous studies.[59–61] Sun et al. showed that a part of water molecules could form hydrogen bonds with hydrophilic groups of corn stalk evaporator to weaken the van der Waals force between water molecules, leading to the reduction of water evaporation enthalpy by ca. 60%.[60] Dong et al. found that the formation of water cluster in UiO-66-COOH nanochannels lowered down water evaporation enthalpy by ca. 45%.[61]

2.4. Interfacial solar steam generation using other water sources

The interfacial solar steam generation of NCF was additionally studied by using different types of water sources, e.g., organic dye (i.e., rhodamine B (RB) or methylene blue (MB))–polluted water, river water, sewage, pool water, lake water, and seawater (Figures S16–S20). Overall, the evaporation rates in these cases keep above 2.2 kg m^{-2} h^{-1} (**Figure 8**a). Figure 8b shows the UV-Vis absorption spectra of dye-polluted water (i.e., RB or MB with a concentration of 20 mg L^{-1}) before and after evaporation. Notably, the condensed water becomes colorless observed by naked eyes, and the dye removal efficiency by NCF is higher than 99.9%. After 6 cycles, the evaporation rate of NCF remains as 2.36 kg m^{-2} h^{-1} (Figure S21), close to that of the first cycle (2.4 kg m^{-2} h^{-1}), indicating the good durability of NCF. Moreover, the dye removal efficiency is not affected by the MB concentration (Figure S22). Beyond this, NCF shows steady evaporation rates of 2.3–2.4 kg m^{-2} h^{-1} under strong acid (pH = 1) or alkali (pH = 13) solution (Figure 8c). The pH values of purified water are close to 7 (Figure 8d), indicating the potential application of NCF in disposing acid/alkali wastewater with a wide pH range.

Additionally, there are no oil droplets in the collected water obtained by solar evaporation of oil/water mixture (i.e.,

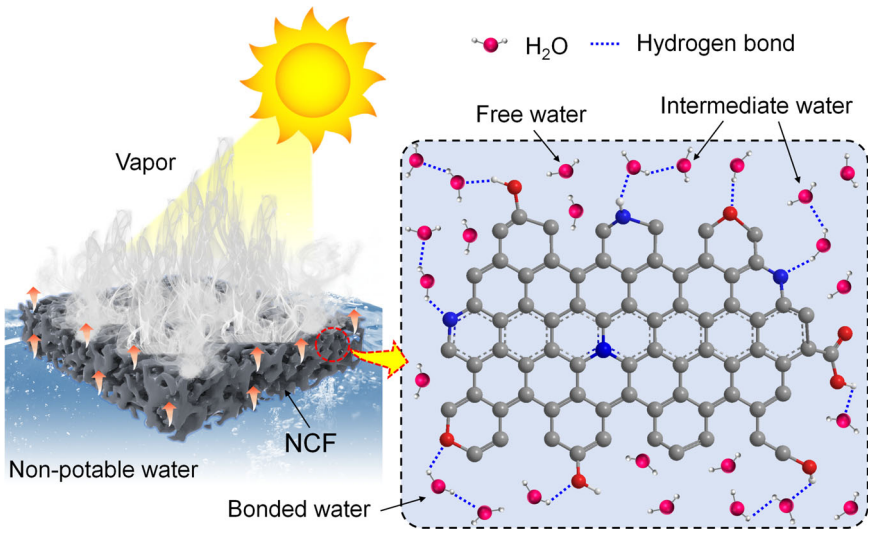

Figure 7. Scheme of possible mechanism on the interfacial solar evaporation of NCF.

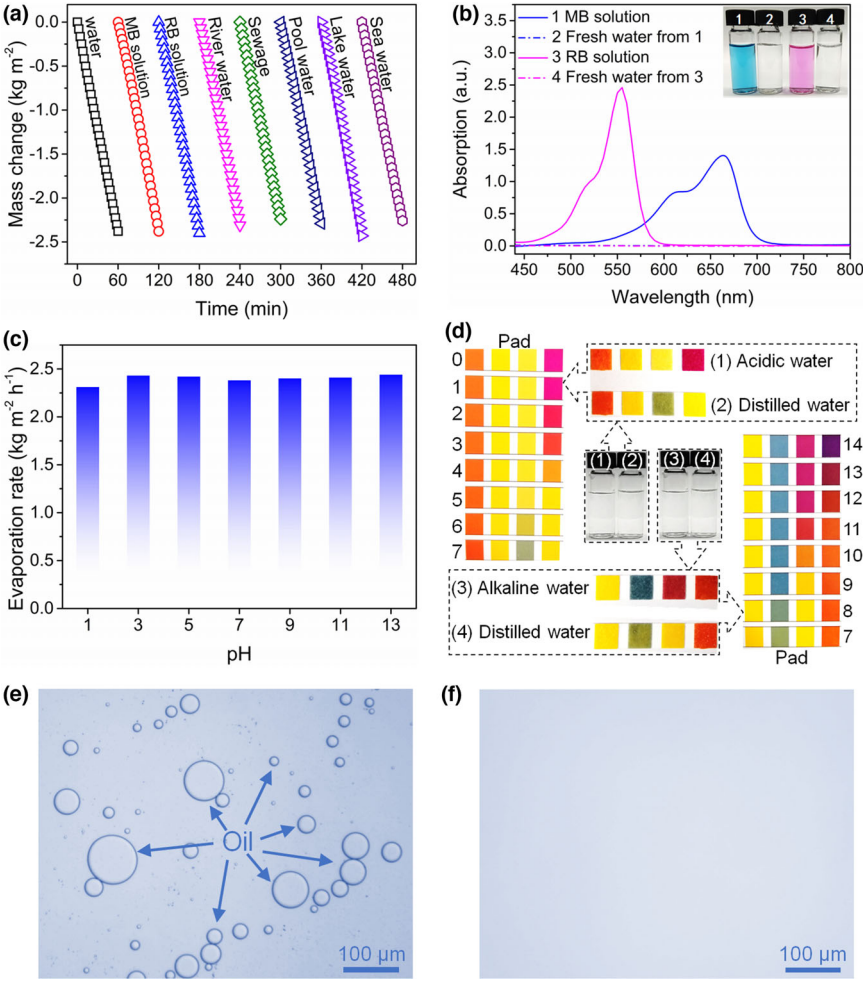

Figure 8. a) Time-dependent mass change curves of NCF using different types of water sources. b) UV-Vis absorption spectra and photographs of dye-polluted water and purified water. c) Evaporation rates of NCF using water with pH values of 1–13. d) Photographs of pH test papers for acidic/alkaline water before and after solar evaporation. Optical images of e) the oil/water mixture and f) the collected freshwater.

dimethylpolysiloxane = 10 000 ppm, Figure 8e,f). The evaporation rate of NCF remains as high as 2.4 kg m^{-2} h^{-1}, which evidently benefits from the superlipophobicity of NCF. A real-world seawater sample from Bohai Sea (China) was employed to study the solar desalination capability of NCF (Figure S17). The concentrations of all four primary ions (i.e., Na^+, Mg^{2+}, K^+ and Ca^{2+}) in the condensed water are two or three orders of magnitude lower than those of seawater (Figure S23), significantly below the drinking water standards defined by the World Health Organization (1000 ppm), or the concentration values obtained by conventional membrane-based (10–500 ppm) seawater purification techniques.[62] The durability of solar evaporators is also highly important during solar desalination. Upon continuous desalination for 20 h, the evaporation rates of 2.2–2.4 kg m^{-2} h^{-1} are maintained (**Figure 9**a). No accumulated salts are observed on the surface of NCF (Figure 9b). Even when the brine water of Chaka Salt Lake (China) is tested, the evaporation rate remains up to 2.1 kg m^{-2} h^{-1} (Figures S24 and S25).

The results above prove the good long-term stability and self-cleaning capability of NCF, which appear to arise from two aspects. Firstly, the micron-sized pores of NCF guarantee the quick diffusion of water towards the evaporator surface to replenish the vaporized salt water. Secondly, the salt concentration gradient, which is formed due to the diverse hydraulic conductivity, drives the dissolution of salt in the microchannels back to the bulk water, realizing spontaneous interchannel salt interchange. As a concept of proof, a model evaporation experiment was conducted, in which solid NaCl (0.5 g) was added on the surface of NCF. It is observed that NaCl gradually dissolves and diffuses back to the bulk water after 50 min (Figure 9c). To sum up, the timely self-renewal of NCF ensures the good long-term durability and excellent reusability.

2.5. Outdoor solar seawater desalination

To certify the practical application of NCF in seawater desalination under natural sunlight, a prototype of a large-scale NCF-based solar steam generation device was designed, which is mainly composed of the evaporation chamber, solar evaporator assembled by four pieces of NCF, vapor condenser,

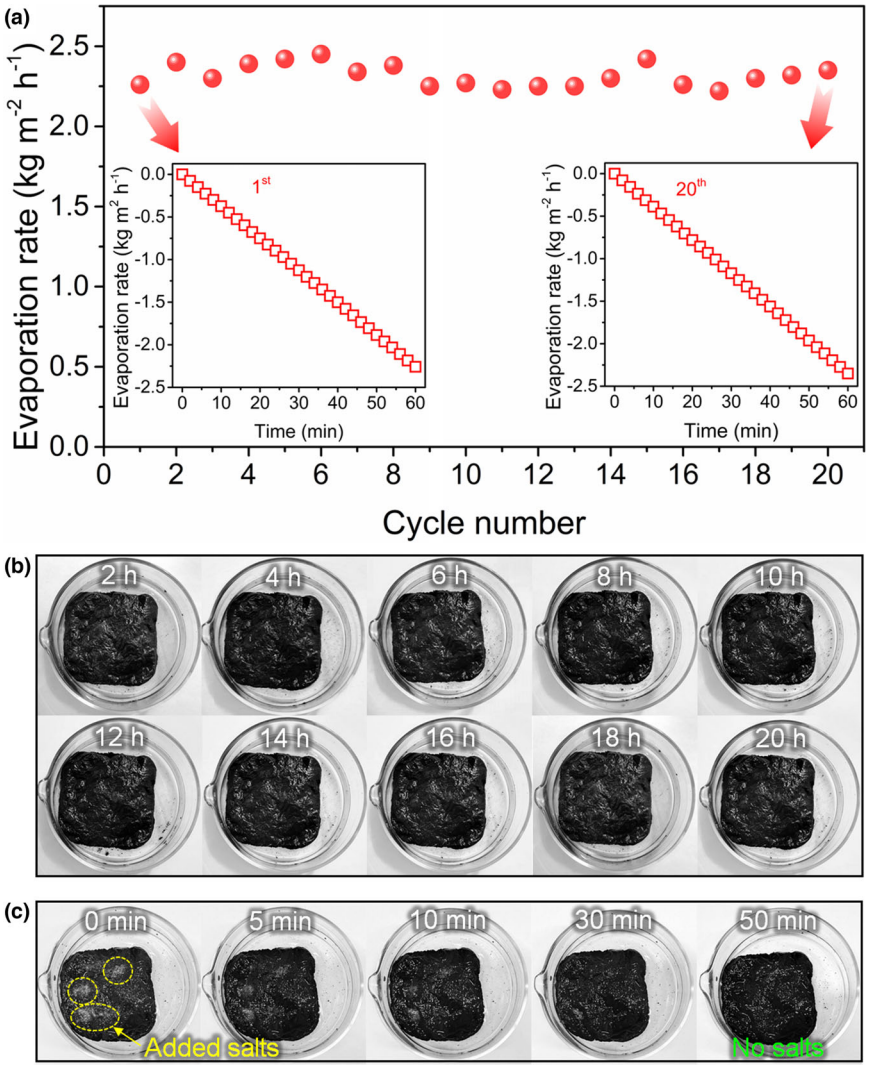

Figure 9. a) Long-term stability of NCF in seawater evaporation for 20 cycles (1 h for one cycle). Insets: the water mass changes using NCF in 1st and 20th cycles. b) Digital images of NCF during seawater evaporation for 20 cycles. c) Photographs of salt ablation process on the surface of NCF.

and water collector troughs (**Figure 10**a–d). The solar desalination device was placed on the roof of Eastern Chemistry Building at Huazhong University of Science and Technology (November 2020). The transparent poly(methyl methacrylate) cover can condense the evaporated water and subsequently converges freshwater to bottom outlet pipe. After 30 min of evaporation, numerous water droplets are observed on the inner surface of the cover (Figure 10e–g). The sunlight intensity and environmental temperature are recorded during the testing from 8:00 to 18:00 (Figure 10h). The maximum solar intensity and temperature values are 0.36 kW m^{-2} and 23 °C, respectively (Figure 10h). The evaporation system exhibits the highest water production rate of 1.05 kg m^{-2} h^{-1} at 14:00 and realizes an accumulated water production of 6.3 kg m^{-2} after 11 h evaporation (Figure 10i). Consequently, the freshwater produced from a 1 m^2 device is enough for the two person's daily water consumption (ca. 5 L). Importantly, the cost of four pieces of NCF is as low as ca. ¥ 8.4 (Table S3). The outdoor solar desalination results demonstrate that the good water purification and scalability of NCF for solar evaporation and desalination.

3. Conclusion

In summary, we have prepared superhydrophilic, self-floating NCF through the low-temperature carbonization of PET waste by adopting melamine and molten salts at 340 °C. The resultant NCF possesses 3D interconnected porous structure, rich N,O-containing functional groups, super-wetting, and ultra-low thermal conductivity of 0.0599 W m^{-1} K^{-1}, which endow NCF with broadband and strong light absorption (98%–99%) and good solar-to-thermal conversion. NCF not only reduces heat loss, but also accelerates water transport and promotes the formation of water cluster to reduce water evaporation enthalpy by ca. 37%. Consequently, NCF exhibits a high evaporation rate (2.4 kg m^{-2} h^{-1}), which is superior to many high-performance photothermal materials. Additionally, NCF functions well using lake water, dye-polluted water, river water, sewage, pool water, seawater, oil/water mixture, and brine water to produce freshwater, with excellent long-term stability and salt-resistance. Finally, a large-scale solar desalination device based on NCF is designed for outdoor experiments. The daily drinkable freshwater production amount is up to 6.3 kg m^{-2}. This work provides a sustainable method to prepare cost-efficient carbon foams from plastic wastes for interfacial solar evaporation, which contributes to addressing global energy crisis and freshwater shortage as well as eliminating waste plastics.

4. Experimental Section

Chemicals and materials: Discarded PET bottles were cleaned and clipped into small sheets. NaCl, rhodamine B (RB), $ZnCl_2$, methylene blue (MB), melamine, and other chemicals were purchased from a commercial reagent company. PET was supplied by Shandong Usolf Company (China). Lake water and seawater were obtained from Donghu lake (Wuhan, Figure S16) and Bohai Sea (China, Figure S17), respectively. River water, pool water, and sewage were collected from the Campus of Huazhong University of Science and Technology (Figures S18–S20). Brine water was collected from Chaka Salt Lake (China, Figure S24).

Synthesis of NCF: As exhibited in Figure 1, 1.5 g PET was evenly mixed with 0.75 g melamine and 3 g $ZnCl_2$/NaCl (=58/42, based on Fechler's work[63]). Subsequently, the mixture was added in a square alumina and carbonized at 340 °C for 30 min in a muffle furnace at the heating rate of 10 °C min^{-1}. Lastly, the product was purified thoroughly using dilute hydrochloric acid solution and then deionized water, dried and finally marked as NCF. Note: the carbonization temperature (340 °C), the mass ratio of melamine to PET (0.5), and the mass ratio of molten salts to PET (2) were optimal values, based on our preliminary results

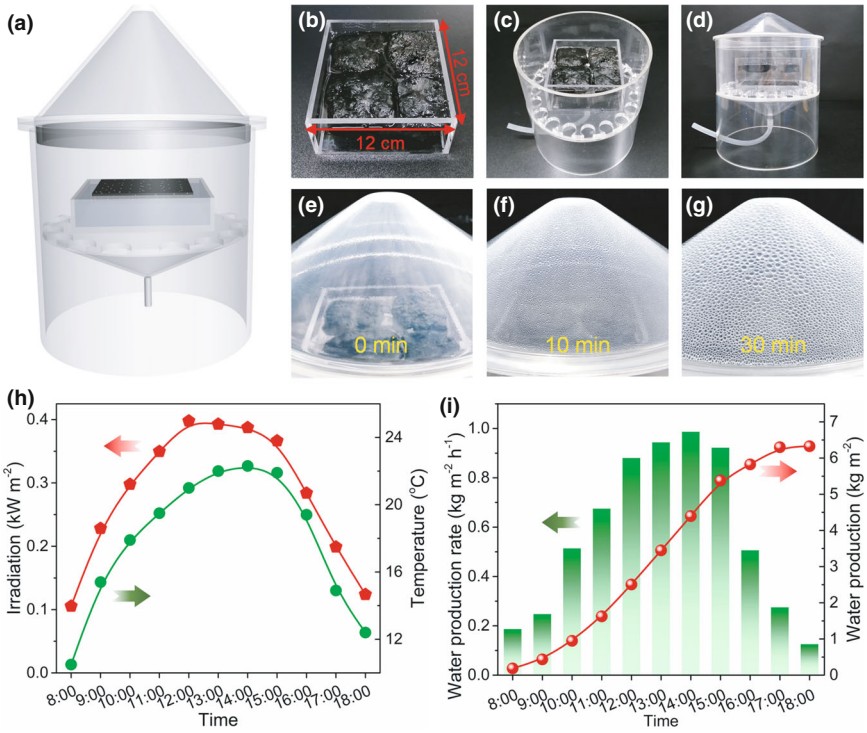

Figure 10. a) Scheme and b–d) photographs of a large-scale NCF-based outdoor solar desalination device. e–g) Photographs of evaporation chamber for freshwater generation over different daytime. h) Sunlight intensity and temperature in the daytime. i) Water production rate and accumulated water production in the daytime.

(Table S1). Likewise, W-NCF was prepared from the carbonization of waste PET under similar experimental conditions (Figure S26). By contrast, 20 mg gridded N, O dual-doped carbon foam (NC) powder was added to 25 mL of ethanol and then sonicated for 5 min. The dispersion was filtered onto a hydrophilic poly (vinylidene fluoride) (PVDF) membrane (diameter = 50 mm, pore size = 0.22 μm) using a vacuum pump to prepare NC@PVDF membrane.

Characterization: Crystalline structure was studied by X-ray diffraction (XRD, SmartLab-SE) and a confocal Raman microscope (in Via Reflex). The field-emission scanning electron microscope (SEM) was conducted on SU8010. The high-resolution transmission electron microscope (HRTEM) was performed on Tecnai G2 F30. Functional groups were studied using Fourier-transform infrared (FT-IR) spectroscopy (BRUKER Vertex 80 FT-IR). Contact angle measurement was conducted on micro-optical contact angle (Dataphysics OCA15EC). X-ray photoelectron spectroscopy (XPS) was performed on VG ESCALAB MK II spectrometer. The elemental content was measured using as elemental analyzer (Vario EL III). Inductively coupled plasma-optical emission spectrometer (ICP-OES) was performed on Agilent 720ES. The absorption spectrum was measured by UV-Vis-NIR spectrophotometer (Lambda 750 S). The UV-Vis absorption spectrum was collected from UV-6100 spectrometer (METASH). The Optical image was obtained by optical microscope (Mshot, MS60). Thermal conductivity was measured by a thermal conductivity analyzer (Hot Disk, TPS 2500). The porosity of NCF was measured according to N_2 physisorption isotherms at 77 K on Micromeritics ASAP 2460. The quench solid density functional theory (DFT) model or Barret-Joyner-Halenda (BJH) model was applied to analyze the pore size distribution. The specific surface area was calculated using Brunauer-Emmett-Teller (BET) equation. Mercury intrusion porosimetry measurement of NCF was conducted to measure the porosity and pore size distribution with an AutoPore V 9600 device (Micromeritics).

Interfacial solar steam generation: Solar steam evaporation experiment was performed by adopting a xenon light (CEL-S500L, CEAULIGHT, Figure S11). NCF floated on the surface of water in a glass crystallizing dish. The surface temperature of NCF was detected by an infrared camera (DMI220). The water mass reduction was real-time monitored by an electronic balance (accuracy = 1 mg, JA2003). During the indoor solar evaporation tests, the relative humidity of the environment was controlled as ca. 32% by using a dehumidifier (DYD-E12A3, Deye, China). Subsequently, we calculated the evaporation rate (m, kg m^{-2} h^{-1}) and solar-to-vapor conversion efficiency (η, %) by employing Equation 2 and 3, respectively:

$$m = \Delta m/(S \times t) \quad (2)$$

$$\eta = m' \times h_{Lv}/(3600 \times P_{in}) \quad (3)$$

where Δm represents the water mass reduction in 1 h (kg), t stands for the irradiation time (1 h), S represents the evaporator area (m^2), m' stands for the evaporation rate under irradiation after subtracting dark evaporation rate (kg m^{-2} h^{-1}), h_{Lv} represents the water evaporation enthalpy (e.g., 2434 kJ kg^{-1} for bulk water), and P_{in} represents the irradiation intensity (0.5–3 kW m^{-2}). Solar evaporation experiment in the absence of evaporators was also conducted and marked as "Blank".

Acknowledgements

The authors would like to thank the reviewers for their kind and valuable comments. The present work is supported by National Natural Science Foundation of China (No. 51903099 and 51991353), 100 Talents Program of Hubei Provincial Government, Huazhong University of Science and Technology (No. 3004013134 and 2021XXJS036), the Innovation and Talent Recruitment Base of New Energy Chemistry and Device (No. B21003), and the Open Research Fund of State Key Laboratory of Polymer Physics and Chemistry, Changchun Institute of Applied Chemistry, Chinese Academy of Sciences. They are grateful to the Analytical and Testing Centre of HUST for access to their facilities. They would like to thank Prof. Qiang Zhao for access to his facilities.

Conflict of Interests

The authors declare no conflict of interests.

Supporting Information

Supporting Information is available from the Wiley Online Library or from the author.

Keywords

carbon foam, solar desalination, solar energy, solar steam generator, waste plastics

Received: April 14, 2021
Revised: May 17, 2021
Published online: June 23, 2021

[1] S. Cao, P. Rathi, X. Wu, D. Ghim, Y.-S. Jun, S. Singamaneni, *Adv. Mater.* **2021**. https://doi.org/10.1002/adma.202000922
[2] P. Tao, G. Ni, C. Song, W. Shang, J. Wu, J. Zhu, G. Chen, T. Deng, *Nat. Energy* **2018**, 3, 1031.

[3] L. Zhu, T. Ding, M. Gao, C. K. N. Peh, G. W. Ho, *Adv. Energy Mater.* **2019**, *9*, 1900250.
[4] M. Gao, L. Zhu, C. K. Peh, G. W. Ho, *Energy Environ. Sci.* **2019**, *12*, 841.
[5] L. Zhu, M. Gao, C. K. N. Peh, X. Wang, G. W. Ho, *Adv. Energy Mater.* **2018**, *8*, 1702149.
[6] T. Ding, Y. Zhou, W. L. Ong, G. W. Ho, *Mater. Today* **2021**, *42*, 178.
[7] X. Zhou, Y. Guo, F. Zhao, G. Yu, *Acc. Chem. Res.* **2019**, *52*, 3244.
[8] Y. Wang, X. Wu, T. Gao, Y. Lu, X. Yang, G. Y. Chen, G. Owens, H. Xu, *Nano Energy* **2021**, *79*, 105477.
[9] X. Wu, T. Gao, C. Han, J. Xu, G. Owens, H. Xu, *Sci. Bull.* **2019**, *64*, 1625.
[10] W. Wang, Y. Shi, C. Zhang, S. Hong, L. Shi, J. Chang, R. Li, Y. Jin, C. Ong, S. Zhuo, P. Wang, *Nat. Commun.* **2019**, *10*, 3012.
[11] Y. Zhou, T. Ding, M. Gao, K. H. Chan, Y. Cheng, J. He, G. W. Ho, *Nano Energy* **2020**, *77*, 105102.
[12] M.-Q. Yang, C. F. Tan, W. Lu, K. Zeng, G. W. Ho, *Adv. Funct. Mater.* **2020**, *30*, 2004460.
[13] X. Wu, Z. Wu, Y. Wang, T. Gao, Q. Li, H. Xu, *Adv. Sci.* **2021**, *8*, 202002501.
[14] Y. Wang, X. Wu, X. Yang, G. Owens, H. Xu, *Nano Energy* **2020**, *78*, 105269.
[15] W. Xu, Y. Xing, J. Liu, H. Wu, Y. Cui, D. Li, D. Guo, C. Li, A. Liu, H. Bai, *ACS Nano* **2019**, *13*, 7930.
[16] L. Zhang, B. Tang, J. Wu, R. Li, P. Wang, *Adv. Mater.* **2015**, *27*, 4889.
[17] X. Wang, Q. Liu, S. Wu, B. Xu, H. Xu, *Adv. Mater.* **2019**, *31*, 1807716.
[18] Y. Xu, J. Wang, F. Yu, Z. Guo, H. Cheng, J. Yin, L. Yan, X. Wang, *ACS Sustainable Chem. Eng.* **2020**, *8*, 12053.
[19] L. Zhou, Y. Tan, D. Ji, B. Zhu, P. Zhang, J. Xu, Q. Gan, Z. Yu, J. Zhu, *Sci. Adv.* **2016**, *2*, e1501227.
[20] C. Wang, Z. Li, W. Wang, R. Xia, X. Ling, *J. Mater. Chem. A* **2019**, *7*, 13080.
[21] B. Shao, Y. Wang, X. Wu, Y. Lu, X. Yang, G. Y. Chen, G. Owens, H. Xu, *J. Mater. Chem. A* **2020**, *8*, 11665.
[22] K. Li, T.-H. Chang, Z. Li, H. Yang, F. Fu, T. Li, J. S. Ho, P.-Y. Chen, *Adv. Energy Mater.* **2019**, *9*, 1901687.
[23] Y. Kuang, C. Chen, S. He, E. M. Hitz, Y. Wang, W. Gan, R. Mi, L. Hu, *Adv. Mater.* **2019**, *31*, 1900498.
[24] Q.-Y. Wu, C. Wang, R. Wang, C. Chen, J. Gao, J. Dai, D. Liu, Z. Lin, L. Hu, *Adv. Energy Mater.* **2020**, *10*, 1902590.
[25] Y. Wang, X. Wu, B. Shao, X. Yang, G. Owens, H. Xu, *Sci. Bull.* **2020**, *65*, 1380.
[26] Q. Zhang, H. Yang, X. Xiao, H. Wang, L. Yan, Z. Shi, Y. Chen, W. Xu, X. Wang, *J. Mater. Chem. A* **2019**, *7*, 14620.
[27] H. Ren, M. Tang, B. Guan, K. Wang, J. Yang, F. Wang, M. Wang, J. Shan, Z. Chen, D. Wei, H. Peng, Z. Liu, *Adv. Mater.* **2017**, *29*, 1702590.
[28] X. Hu, W. Xu, L. Zhou, Y. Tan, Y. Wang, S. Zhu, J. Zhu, *Adv. Mater.* **2017**, *29*, 1604031.
[29] C. Wang, J. Wang, Z. Li, K. Xu, T. Lei, W. Wang, *J. Mater. Chem. A* **2020**, *8*, 9528.
[30] H. Liang, Q. Liao, N. Chen, Y. Liang, G. Lv, P. Zhang, B. Lu, L. Qu, *Angew. Chem. Int. Ed.* **2019**, *58*, 19041.
[31] J. Li, X. Wang, Z. Lin, N. Xu, X. Li, J. Liang, W. Zhao, R. Lin, B. Zhu, G. Liu, L. Zhou, S. Zhu, J. Zhu, *Joule* **2020**, *4*, 928.
[32] X. Shan, Y. Lin, A. Zhao, Y. Di, Y. Hu, Y. Guo, Z. Gan, *Nanotechnology* **2019**, *30*, 425403.
[33] P. Qiu, F. Liu, C. Xu, H. Chen, F. Jiang, Y. Li, Z. Guo, *J. Mater. Chem. A* **2019**, *7*, 13036.
[34] X. Zhou, F. Zhao, Y. Guo, B. Rosenberger, G. Yu, *Sci. Adv.* **2019**, *5*, eaaw5484.
[35] F. Zhao, X. Zhou, Y. Shi, X. Qian, M. Alexander, X. Zhao, S. Mendez, R. Yang, L. Qu, G. Yu, *Nat. Nanotechnol.* **2018**, *13*, 489.
[36] Q.-F. Guan, Z.-M. Han, Z.-C. Ling, H.-B. Yang, S.-H. Yu, *Nano Lett.* **2020**, *20*, 5699.
[37] A. J. Martín, C. Mondelli, S. D. Jaydev, J. Pérez-Ramírez, *Chem* **2021**, *7*, 1487.
[38] F. Tian, Y. Yang, X.-L. Wang, W.-L. An, X. Zhao, S. Xu, Y.-Z. Wang, *Mater. Horiz.* **2019**, *6*, 1733.
[39] N. Cai, S. Xia, X. Zhang, Z. Meng, P. Bartocci, F. Fantozzi, Y. Chen, H. Chen, P. T. Williams, H. Yang, *Chemsuschem* **2020**, *13*, 938.
[40] X. Jie, W. Li, D. Slocombe, Y. Gao, I. Banerjee, S. Gonzalez-Cortes, B. Yao, H. AlMegren, S. Alshihri, J. Dilworth, J. Thomas, T. Xiao, P. Edwards, *Nat. Catal.* **2020**, *3*, 902.
[41] D. X. Luong, K. V. Bets, W. A. Algozeeb, M. G. Stanford, C. Kittrell, W. Chen, R. V. Salvatierra, M. Ren, E. A. McHugh, P. A. Advincula, Z. Wang, M. Bhatt, H. Guo, V. Mancevski, R. Shahsavari, B. I. Yakobson, J. M. Tour, *Nature* **2020**, *577*, 647.
[42] J. Gong, X. Chen, T. Tang, *Prog. Polym. Sci.* **2019**, *94*, 1.
[43] T. Tang, X. Chen, X. Meng, H. Chen, Y. Ding, *Angew. Chem. Int. Ed.* **2005**, *44*, 1517.
[44] J. Gong, K. Yao, J. Liu, Z. Jiang, X. Chen, X. Wen, E. Mijowska, N. Tian, T. Tang, *J. Mater. Chem. A* **2013**, *1*, 5247.
[45] J. Gong, J. Liu, X. Chen, Z. Jiang, X. Wen, E. Mijowska, T. Tang, *J. Mater. Chem. A* **2015**, *3*, 341.
[46] Y. Wen, K. Kierzek, X. Chen, J. Gong, J. Liu, R. Niu, E. Mijowska, T. Tang, *Waste Manage.* **2019**, *87*, 691.
[47] B. Zhang, C. Song, C. Liu, J. Min, J. Azadmanjiri, Y. Ni, R. Niu, J. Gong, Q. Zhao, T. Tang, *J. Mater. Chem. A* **2019**, *7*, 22912.
[48] C. Song, L. Hao, B. Zhang, Z. Dong, Q. Tang, J. Min, Q. Zhao, R. Niu, J. Gong, T. Tang, *Sci. China Mater.* **2020**, *63*, 779.
[49] N. Liu, L. Hao, B. Zhang, R. Niu, J. Gong, T. Tang, *Sustainable Energy Fuels* **2020**, *4*, 5522.
[50] C. Song, B. Zhang, L. Hao, J. Min, N. Liu, R. Niu, J. Gong, T. Tang, Green. *Energy Environ.* **2021**. https://doi.org/10.1016/j.gee.2020.10.002
[51] J. S. Yeon, Y. H. Ko, T. H. Park, H. Park, J. Kim, H. S. Park, *Energy Environ. Mater.* **2021**. https://doi.org/10.1002/eem2.12187
[52] Y. Feng, S. Chen, D. Shen, J. Zhou, B. Lu, *Energy Environ. Mater.* **2021**. https://doi.org/10.1002/eem2.12126
[53] L. Liu, T. Ma, W. Fang, Y. Liu, K. Konstantinov, J. Wang, H.-K. Liu, *Energy Environ. Mater.* **2021**, *4*, 239.
[54] C. Shu, Z. Gan, Y. Hou, T. Zhu, J. Ma, W. Tang, Y. Wu, *Energy Environ. Mater.* **2021**, *4*, 81.
[55] N. Liu, L. Hao, B. Zhang, R. Niu, J. Gong, T. Tang, *Energy Environ. Mater.* **2021**. https://doi.org/10.1002/eem2.12199
[56] P. He, L. Hao, N. Liu, H. Bai, R. Niu, J. Gong, *Chem. Eng. J.* **2021**, *423*, 130268.
[57] M. T. Rodgers, P. B. Armentrout, *J. Phys. Chem. A* **1997**, *101*, 1238.
[58] X. Li, Z.-Z. Yang, *J. Phys. Chem. A* **2005**, *109*, 4102.
[59] J. Tang, T. Zheng, Z. Song, Y. Shao, N. Li, K. Jia, Y. Tian, Q. Song, H. Liu, G. Xue, A. C. S. Appl, *Mater. Interfaces* **2020**, *12*, 18504.
[60] Z. Sun, W. Li, W. Song, L. Zhang, Z. Wang, *J. Mater. Chem. A* **2020**, *8*, 349.
[61] Z. Dong, C. Zhang, H. Peng, J. Gong, Q. Zhao, *J. Mater. Chem. A* **2020**, *8*, 24493.
[62] S. P. Surwade, S. N. Smirnov, I. V. Vlassiouk, R. R. Unocic, G. M. Veith, S. Dai, S. M. Mahurin, *Nat. Nanotechnol.* **2015**, *10*, 459.
[63] N. Fechler, T.-P. Fellinger, M. Antonietti, *Adv. Mater.* **2013**, *25*, 75.

